PHYSICAL REVIEW D **83,** 122002 (2011)

Time domain simulations of arm locking in LISA

J. I. Thorpe,[1,*] P. Maghami,[2] and J. Livas[1]

[1]*Gravitational Astrophysics Laboratory, NASA Goddard Space Flight Center, 8800 Greenbelt Road, Greenbelt, Maryland 20771, USA*

[2]*Attitude Control Systems Engineering Branch, NASA Goddard Space Flight Center, 8800 Greenbelt Road, Greenbelt, Maryland 20771, USA*

(Received 26 February 2011; published 1 June 2011)

Arm locking is a proposed laser frequency stabilization technique for the Laser Interferometer Space Antenna (LISA), a gravitational-wave observatory sensitive in the milliHertz frequency band. Arm locking takes advantage of the geometric stability of the triangular constellation of three spacecraft that compose LISA to provide a frequency reference with a stability in the LISA measurement band that exceeds that available from a standard reference such as an optical cavity or molecular absorption line. We have implemented a time-domain simulation of a Kalman-filter–based arm-locking system that includes the expected limiting noise sources as well as the effects of imperfect *a priori* knowledge of the constellation geometry on which the design is based. We use the simulation to study aspects of the system performance that are difficult to capture in a steady-state frequency-domain analysis such as frequency pulling of the master laser due to errors in estimates of heterodyne frequency. We find that our implementation meets requirements on both the noise and dynamic range of the laser frequency with acceptable tolerances and that the design is sufficiently insensitive to errors in the estimated constellation geometry that the required performance can be maintained for the longest continuous measurement intervals expected for the LISA mission.

DOI: 10.1103/PhysRevD.83.122002 PACS numbers: 04.80.Nn, 07.05.Dz, 07.05.Tp, 95.55.Ym

I. INTRODUCTION

The Laser Interferometer Space Antenna (LISA) [1,2] is a planned facility for observing gravitational radiation in the milliHertz frequency band, a regime rich in astrophysical sources. The LISA measurement concept [2] calls for laser interferometry to be used to measure fluctuations in the distance between freely falling test masses contained within spacecraft separated by $\sim 5 \times 10^9$ m with a precision of $\sim 10 \times 10^{-12}$ m, or ~ 10 pm. The interferometric measurements are performed as a series of one-way measurements between pairs of spacecraft (SC) and then combined using a technique known as time delay interferometry (TDI) [3,4] to form observables that suppress laser frequency noise while retaining gravitational wave signals.

The capability of TDI to reject laser frequency noise is chiefly limited by imperfect knowledge of the absolute light travel times between the spacecraft (often referred to as the "arm lengths"), which is expected to have an accuracy of ~ 1 m or ~ 3 ns. With this level of arm-length accuracy, the contribution of laser frequency noise in the TDI observables will satisfy the allocated equivalent path length noise of 2.5 pm/$\sqrt{\mathrm{Hz}}$ so long as the input laser frequency noise does not exceed a level of

$$\tilde{\nu}_{\text{pre-TDI}}(f) = \left(282\,\frac{\mathrm{Hz}}{\sqrt{\mathrm{Hz}}}\right) \cdot \sqrt{1 + \left(\frac{2.8\ \mathrm{mHz}}{f}\right)^4}, \qquad (1)$$

where the Fourier frequency f ranges over the LISA measurement band, $0.1\ \mathrm{mHz} \leq f \leq 0.1$ Hz. The expected free-running noise level of the LISA lasers in the measurement band is roughly $10\ \mathrm{kHz}/\sqrt{\mathrm{Hz}} \cdot (1\ \mathrm{Hz}/f)$, which exceeds the requirement in (1) by more than 4 orders of magnitude at the low end of the LISA band. Consequently, the lasers must be stabilized using an external frequency reference. A number of candidate stabilization schemes have been studied and determined to be viable from a noise performance perspective [5,6]. The current focus is on evaluating other aspects of each candidate scheme such as complexity, robustness to implementation errors, and operational constraints so that the most effective design can be selected.

Two of the candidate schemes rely on arm locking, which utilizes the existing LISA science signals to derive a frequency reference from the geometry of the constellation. In one scheme, arm locking is the sole method employed to stabilize the laser frequency where in the other it is combined with another stabilization method in a hybrid system. We focus on the latter case in this paper.

Since its original introduction [7], the arm-locking concept has been refined [8,9] leading to improvements in its expected performance. Arm locking has also been studied in a number of hardware models [10–12], which have helped to identify potential implementation issues that were not readily apparent from frequency-domain studies of arm locking. Chief among these was the discovery that the inability to predict the heterodyne frequencies of the LISA science signals due to imperfect knowledge of the interspacecraft Doppler shifts leads to "frequency pulling" of the

*james.i.thorpe@nasa.gov

arm locked laser. If not properly mitigated, this frequency pulling can be so severe that the laser exceeds its dynamic range in a matter of hours.

In this paper we present the results from a series of time-domain simulations of arm locking. The goal is to combine the attractive features of the frequency-domain models (realistic noise sources, orbit models, etc.) with those of the hardware models (sensitivity to transients, nonlinearities, etc.). The rest of the paper is organized as follows. In Sec. II we describe the problem of arm locking in LISA, defining the relevant signals. In Sec. III we briefly review the frequency-pulling effect. We discuss our particular arm-locking design and the technical details of our simulation in Sec. IV and present results in Sec. V.

II. ARM-LOCKING MODEL

To maintain the focus on the arm-locking dynamics, we make a few simplifications in our model of the LISA interferometry. The first is that we only consider the interferometric measurements made between different SC (the "long-arm" signals) and ignore the additional measurements made between the SC and the proof mass (the "-short-arm" signals). While a combination of both signals is needed to reach the ~10 pm sensitivity levels required for detecting gravitational waves, the ~nm sensitivity level of the long-arm signals is more than sufficient for frequency stabilization at the level of (1).

A second simplification is that we model the two lasers on-board the master SC as a single laser. In reality one of the lasers will be phase locked to the other using a high-gain phase-lock loop. The residual noise in this phase-lock loop is expected to be far below the other noise sources considered in this paper. Readers interested in additional detail on the LISA interferometric measurement concept should consult one of the many overview papers [2,6,13].

A. Notation

Our notation system is an adaptation of that used by McKenzie, *et al.* [9]. The most notable difference is that we represent signals as fluctuations in frequency rather than fluctuations in phase and replace ϕ with ν to reflect this. The three LISA spacecraft (SC) are labeled SC_i, $i = 1, 2, 3$ and it is assumed that SC_1 is the master SC. The many different frequency signals are labeled with both an alphabetic and a numeric subscript. The alphabetic subscript refers to the physical nature of the signal while the numeric subscript refers to the SC involved in producing the signal. In a two digit numeric subscript, the first digit indicates the receiving SC while the second refers to the transmitting SC. For example, ν_{S13} denotes the shot noise on the photoreceiver on-board SC_1 that is receiving signals from SC_3. Table II in the Appendix summarizes the notation used in this paper and, where possible, the corresponding notation in [9].

B. A Single LISA laser link

Figure 1 shows a schematic of the LISA constellation. We begin our analysis of the arm-locking signal chain with Laser 1 on SC_1, which produces light with a frequency ν_{O1}. This frequency is a combination of the intrinsic frequency noise of the laser, ν_{L1}, and the control signal provided by the arm-locking loop. As the laser departs SC_1 in the direction of SC_3, it picks up a Doppler shift due to the motion of SC_1. The magnitude of this Doppler shift is $\lambda^{-1}\vec{V}_1 \cdot \hat{\eta}_{13}$, where λ is the wavelength of the laser, $\vec{V}_1$ is the velocity of SC_1, and $\hat{\eta}_{13}$ is the unit vector along the path from SC_1 to SC_3. For the purposes of calculating Doppler shifts, we make the assumption that $\hat{\eta}_{ij} = -\hat{\eta}_{ji}$ even though the rotation of the constellation causes these angles to differ on the $\sim\mu$ radian level [2].

The laser then experiences a delay of τ_{13} on the order of 5×10^9 m$/c \approx 17$ s as it travels to SC_3. At SC_3, the signal picks up another Doppler term due to the motion of SC_3. At the photoreceiver on SC_3 it is interfered with the local laser (with frequency ν_{O3}) to generate an electrical heterodyne signal with frequency

$$\nu_{H31}(t) = \nu_{O3}(t) - \nu_{O1}(t - \tau_{13}) - \lambda^{-1}[\vec{V}_1(t - \tau_{13}) - \vec{V}_3(t)] \cdot \hat{\eta}_{13} + \nu_{S31}(t), \qquad (2)$$

where ν_{S31} is a shot noise contribution due to the low light level of the received beam. A device we will refer to as the "frequency meter" (although it is more commonly called a phase meter [14]) is used to measure the frequency of the heterodyne signal. The first step is digitization, which introduces a noise term due to fluctuations in the frequency of the oscillator used to drive the digitizers. To first order, this clock noise is additive with a spectral density that is proportional to the instantaneous heterodyne frequency,

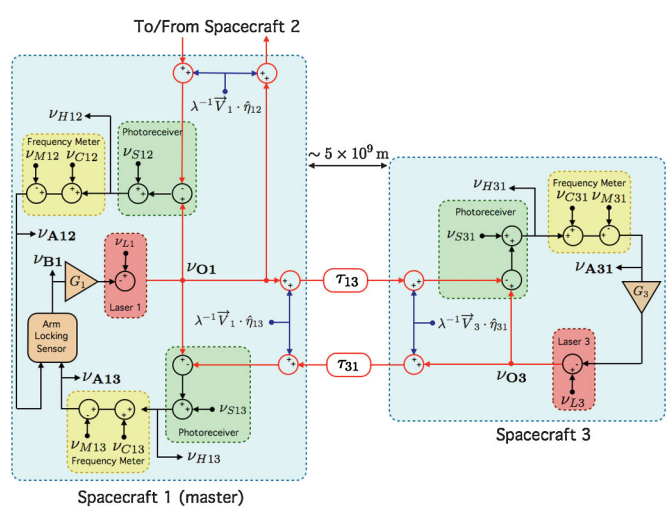

FIG. 1 (color). Schematic of frequency signals relevant to arm locking. See Sec. II of the text for details and the Appendix for a key to notation. Adapted from Fig. 1 of [9].

$$\tilde{\nu}_{C31}(f) \equiv \nu_{H31} \cdot \tilde{y}_3(f). \tag{3}$$

Here $\tilde{y}_3(f)$ represents the spectrum of fractional frequency fluctuations of the clock on-board SC_3. The frequency meter also measures the frequency of the heterodyne signal relative to some model signal ν_{M31}. The model signal can be used to remove the slow drift of the heterodyne frequency caused by time-varying Doppler shifts or to impose a constant frequency offset in a phase-lock loop. The output of the frequency meter is given by

$$\nu_{A31}(t) = \nu_{H31}(t) - \nu_{M31}(t) + \nu_{C31}(t). \tag{4}$$

C. Doppler shifts

The LISA SC will experience relative velocities along their lines of sight of several meters per second, resulting in Doppler shifts of several MHz. These Doppler shifts are approximately constant in the LISA measurement band and it is convenient to remove them prior to implementing arm locking. We begin by separating the SC velocity terms into a deterministic term arising from the SC orbits ($\vec{V}_{Oi}$) and a stochastic term arising from attitude jitter of the SC ($\delta\vec{V}_i$)

$$\vec{V}_i(t) = \vec{V}_{Oi}(t) + \delta\vec{V}_i(t). \tag{5}$$

This in turn leads to two Doppler contributions in the heterodyne signals ν_{Hij}, an orbital motion term (ν_{Dij}) and a SC jitter term (ν_{Jij}) given by

$$\nu_{Dij}(t) = \lambda^{-1}[\vec{V}_{Oi}(t) - \vec{V}_{Oj}(t - \tau_{ji})] \cdot \hat{\eta}_{ij}, \tag{6}$$

$$\nu_{Jij}(t) = \lambda^{-1}[\delta\vec{V}_i(t) - \delta\vec{V}_j(t - \tau_{ji})] \cdot \hat{\eta}_{ij}. \tag{7}$$

With these signal definitions, the heterodyne signal on-board SC_3 can be written

$$\nu_{H31}(t) = \nu_{O3}(t) - \nu_{O1}(t - \tau_{13}) + \nu_{D31}(t) + \nu_{J31}(t) + \nu_{S31}(t). \tag{8}$$

D. Phase locking on SC_2 and SC_3

Arm locking requires that the slave SC (SC_2 and SC_3 in our example) operate in a transponder mode, returning to the master SC a copy of the light field that was received. This is accomplished by using a phase-lock loop to control the lasers on-board the slave SC. Using SC_3 in Fig. 1 as an example, the controller G_3 adjusts the frequency of Laser 3 to minimize the output of the frequency meter, ν_{A31}. In the Laplace domain, the output of Laser 3 will be

$$\nu_{O3}(s) = \frac{G_3}{1+G_3}[\nu_{M31} + \nu_{O1}(s)e^{-s\tau_{13}} - \nu_{D31}(s) - \nu_{J31}(s) - \nu_{S31}(s) - \nu_{C31}(s)] + \frac{1}{1+G_3}\nu_{L3}(s). \tag{9}$$

Under the assumption of a high-bandwidth phase-lock loop, $G_3 \gg 1$, this simplifies to

$$\nu_{O3}(s) \approx \nu_{M31} + \nu_{O1}(s)e^{-s\tau_{13}} - \nu_{D31}(s) - \nu_{J31}(s) - \nu_{S31}(s) - \nu_{C31}(s). \tag{10}$$

E. Formation of the arm-locking error signal

The signal from Laser 3 is transmitted back to SC_1, picking up a Doppler contribution form SC_3, a time delay τ_{31}, and a Doppler contribution from SC_1. At SC_1 it is interfered with Laser 1 on a photoreceiver, generating shot noise ν_{S13}. Fluctuations in the heterodyne signal are measured by a frequency meter, which subtracts a model $\nu_{M13}(t)$ and adds a clock noise ν_{C13} to produce the main science signal for the $SC_1 - SC_3$ arm, $\nu_{A13}(t)$. Using (10) to replace ν_{O3}, ν_{A13} can be written as

$$\begin{aligned}\nu_{A13}(t) = {} & [\nu_{O1}(t) - \nu_{O1}(t - \tau_{13} - \tau_{31})] + [\nu_{J13}(t) \\ & + \nu_{J31}(t - \tau_{31})] + [\nu_{S13}(t) + \nu_{S31}(t - \tau_{31})] \\ & + [\nu_{C13}(t) + \nu_{C31}(t - \tau_{31})] + [\nu_{D13}(t) \\ & + \nu_{D31}(t - \tau_{31})] - [\nu_{M13}(t) + \nu_{M31}(t - \tau_{31})].\end{aligned} \tag{11}$$

The second to last bracketed term in (11) represents the deterministic part of the heterodyne signal. The model signal in the frequency meter, $\nu_{M13}(t)$, can be used to remove this term, leaving behind a (hopefully small) residual error term, $\nu_{E13}(t)$,

$$\nu_{M13}(t) = \nu_{D13}(t) + \nu_{D31}(t - \tau_{31}) - \nu_{M31}(t - \tau_{31}) - \nu_{E13}(t). \tag{12}$$

These residual errors lead to frequency pulling of the master laser. Section III presents estimates for the size of these errors. With the deterministic terms (mostly) removed, ν_{A13} can be represented in the Laplace domain as

$$\begin{aligned}\nu_{A13}(s) = {} & \nu_{O1}(s)[1 - e^{-s(\tau_{13}+\tau_{31})}] \\ & + [\nu_{J13}(s) + \nu_{J31}(s)e^{-s\tau_{31}}] \\ & + [\nu_{C13}(s) + \nu_{C31}(s)e^{-s\tau_{31}}] \\ & + [\nu_{S13}(s) + \nu_{S31}(s)e^{-s\tau_{31}}] + \nu_{E13}(s).\end{aligned} \tag{13}$$

The $SC_1 - SC_2$ arm produces a signal, $\nu_{A12}(s)$, that is analogous to $\nu_{A13}(s)$. The arm-locking sensor is a linear combination of these two signals that is used to estimate the Laser 1 fluctuations, ν_{O1}, so that they can be suppressed in a feedback loop. The output of the arm-locking sensor, labeled ν_{B1} in Fig. 1 is given by

$$\nu_{B1} = \mathbf{S}\begin{bmatrix} \nu_{A12} \\ \nu_{A13} \end{bmatrix}, \tag{14}$$

where $\mathbf{S}$ is the arm-locking sensor vector that describes the specific linear combination of the two individual arm

signals. For example, the "common-arm" sensor uses the sensor vector $\mathbf{S}_+ \equiv [\frac{1}{2}, \frac{1}{2}]$. Table I in [9] provides expressions for several arm-locking sensors that have been studied in the literature.

F. Noise levels

1. Intrinsic laser frequency noise

For this work we assume a prestabilized, frequency tunable laser source with a frequency noise spectral density in the LISA band of

$$\tilde{\nu}_L(f) = \left(800\frac{\text{Hz}}{\sqrt{\text{Hz}}}\right)\cdot\sqrt{1+\left(\frac{2.8\ \text{mHz}}{f}\right)^4},$$
$$0.1\ \text{mHz} \le f \le 0.1\ \text{Hz}. \tag{15}$$

This is representative of the noise-floor of the Mach-Zehnder interferometer stabilization system [15] that will fly on LISA Pathfinder [16], a LISA technology demonstrator mission.

2. Shot noise

Shot noise is uncorrelated at each detector and has an equivalent frequency noise spectrum of

$$\tilde{\nu}_S(f) = \sqrt{\frac{hc}{\lambda P_{\text{rec}}}}\left(\frac{\text{Hz}}{\sqrt{\text{Hz}}}\right)\left(\frac{f}{1\ \text{Hz}}\right), \tag{16}$$

where $\lambda = 1064$ nm is the laser wavelength and $P_{\text{rec}} \sim 100$ pW is the received power. For these numbers, (16) gives $\tilde{\nu}_S = 43\ \mu\text{Hz}/\sqrt{\text{Hz}}\cdot(f/1\ \text{Hz})$.

3. Clock noise

The spectral density of the fractional frequency variations of the SC clocks are estimated to be (Table IV of [9])

$$\tilde{y}(f) = 2.4\times 10^{-12}/\sqrt{f}. \tag{17}$$

While LISA will employ a clock-transfer scheme to correct for differential clock noise between the SC [17], we assume that the correction takes place in post processing on the ground and is not applied to the arm-locking error signals on-board the SC.

4. Spacecraft jitter

The spacecraft jitter noise model is based on simulations of the drag-free control performance of LISA [18]. The jitter can be divided into two orthogonal components in the plane of the LISA constellation that are independent. Each of these has a position jitter in the LISA measurement band of

$$\delta\tilde{x}(f) = 2.5\ \text{nm}/\sqrt{\text{Hz}}, \quad 0.1\ \text{mHz} \le f \le 0.1\ \text{Hz}. \tag{18}$$

Note that due to the fact that the interior angle of the constellation is not 90 deg, the spacecraft jitter contributions from SC_1 will be partially correlated in the frequency meter signals $\nu_{A12}(t)$ and $\nu_{A13}(t)$. Finally, we note that it would, in principle, be possible to remove the spacecraft jitter by including the short-arm interferometers in both the phase-lock error signals in the far SC and the arm-locking error signals in the master SC. This would reduce the jitter from ~nm to ~pm in the LISA band. As with the clock noise correction, this would require additional on-board processing and is not necessary to reach the pre-TDI noise requirement specified in (1).

III. LASER FREQUENCY PULLING AND HETERODYNE ESTIMATION

In Sec. II, we explained how Doppler shifts arising from the SC orbits enter the long-arm frequency meter signals and how the deterministic parts of the signals are removed using models of the heterodyne frequency. If we take the expression for the main science signal of the $\text{SC}_1 - \text{SC}_3$ arm, ν_{A13}, as expressed in (13) and consider only the terms resulting from the laser frequency, ν_{O1}, and the errors in the heterodyne estimate, ν_{E13}, the result is

$$\nu_{A13}(s) = \nu_{O1}(s)[1 - e^{-s(t-\tau_{13}-\tau_{31})}] + \nu_{E13}(s).$$

If we take the low frequency limit, $s \to 0$, we find that the first term vanishes. In other words, the signal in ν_{A13} is insensitive to fluctuations in laser frequency at zero frequency. The second term, however, is unaffected. The situation is obviously the same for ν_{A12} and also for any arm-locking sensor formed as a linear combination of ν_{A12} and ν_{A13}. If the arm-locking controller has any gain at zero frequency, it will cause the laser to ramp in an attempt to zero out the heterodyne error terms. This laser frequency pulling can be mitigated by reducing the arm-locking loop gain below the LISA measurement band, although care must be taken to ensure that sufficient gain is still present within the band. The rate of pulling is proportional to the error in the estimate of the heterodyne frequency, hence the design requirements of the control filter will be driven by the accuracy with which the heterodyne frequency can be estimated.

As pointed out by [9], it is convenient to combine the heterodyne models from the individual arms into a common and differential component. For the case where SC_1 is the master SC, the common and differential heterodyne models are

$$\begin{aligned}\nu_{M+}(t) &\equiv \nu_{M12}(t) + \nu_{M13}(t),\\ \nu_{M-}(t) &\equiv \nu_{M12}(t) - \nu_{M13}(t).\end{aligned} \tag{19}$$

It is also expected that arm locking may require periodic reacquisition, either because of an external disturbance (e.g. pointing of the high-gain antenna) or because some component of the arm-locking system is in a nondesirable operating range (e.g. laser near a longitudinal mode transition, arms close to equal, etc.). Consequently, the heterodyne frequency only needs to be estimated for periods on

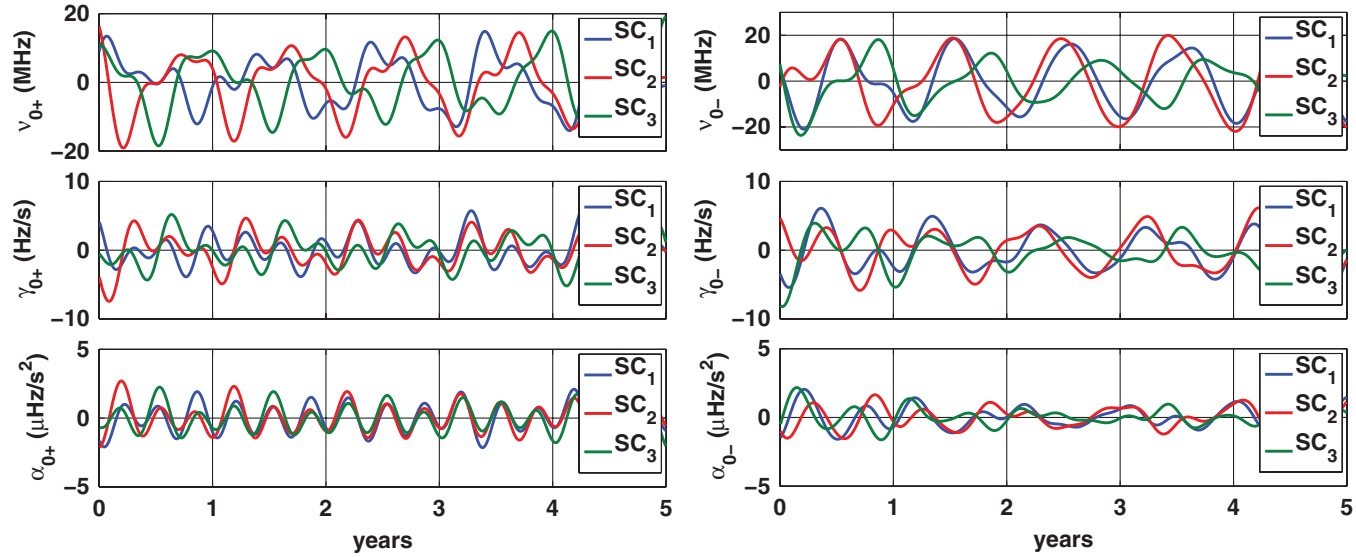

FIG. 2 (color). Constant, linear, and quadratic Doppler parameters for the LISA orbital solution *cf3* in [19]. The three plots on the left show the common-arm Doppler parameters. The three plots on the right show the differential-arm Doppler parameters. Curves labeled SC_i correspond to the case where SC_i is the master SC.

the order of weeks. For such periods, it is appropriate to use a quadratic model,

$$\nu_{Mx}(t) \approx \nu_{0x} + \gamma_{0x}t + \alpha_{0x}t^2, \qquad x = (+, -). \tag{20}$$

A. Expected doppler

Although the models for the heterodyne signals include both Doppler shifts and intentional frequency offsets, the Doppler shifts provide the only source of uncertainty. There are a number of realizations of the LISA orbits that can be used to derive expected Doppler frequencies. All exhibit a primary frequency of $\sim 1\ \mathrm{yr}^{-1}$ with harmonics of various amplitudes. There is also a secular component that tends to degrade the constellation (higher Doppler shifts, larger arm-length mismatches, etc.) as the mission progresses. In Fig. 2 we plot each of the six Doppler parameters in (20) resulting from an orbital solution by Hughes [19] that was optimized to minimize the average Doppler frequency in each arm. Each plot contains three traces, one for each possible choice of master SC.

B. Doppler estimation methods

A number of methods have been proposed for determining the Doppler frequency. One method is to use the orbital ephemeris, such as the one plotted in Fig. 2 to predict the Doppler. With periodic updates to the ephemeris from ranging data taken during normal SC down-link operations, the ephemeris velocities can be expected to be accurate to 3 mm/s [20]. One issue is that the measured velocity is the projected component along the line of sight between Earth and the SC. Transverse velocities are not directly measured but are still constrained by the orbital model. Consequently one would expect that the errors in Doppler estimation could differ by a large amount between different inter-SC links.

Another method for estimating the Doppler frequency is to differentiate the active ranging signal that is used to determine the absolute link lengths for the TDI algorithm. Unlike ground tracking, this method directly measures the velocity along the inter-SC link. Ranging is expected to have position accuracy of $\sim$1 m or better over averaging periods of $\sim$1000 s [21]. This suggests that velocities could be measured to $\sim$mm/s accuracy, corresponding to Doppler frequency errors on the order of $\sim$kHz. Additional processing such as longer averaging, Kalman filtering, or combination with an orbital model may allow for further improvements [22]. In all cases, the processing (including the determination of range from the pseudorandom code) would take place on ground. Consequently there would be some delay before the updated Doppler model could be uploaded to the SC.

McKenzie, *et al.* [9] proposed a simple method for determining the heterodyne frequency directly from the frequency meter data itself. If we consider the expression for the main science signals (11), all of the terms contain

TABLE I. Doppler errors from 200 s averaging of the science signal with Mach-Zehnder stabilized laser frequency noise given by (15). Adapted from Table III of [9]. A * indicates the error was greater than the expected signal and hence the measurement is not used.

Parameter	ν_{0+}	ν_{0-}	γ_{0+}	γ_{0-}	α_{0+}	α_{0-}
Error	45 Hz	0.51 Hz	2.2 Hz/s	0.02 Hz/s	*	*

mean-zero stochastic processes with the exception of the Doppler terms. Applying a simple averaging filter to this signal can suppress the noise terms to reveal the heterodyne frequency. This simple algorithm relies only on information from the master SC and could be easily implemented on-board. Table I gives the errors in the Doppler coefficients estimated by McKenzie, *et al.* assuming a MZ stabilized laser with a frequency noise spectrum given by (15) and a 200 s averaging time.

IV. ARM-LOCKING SIMULATIONS

A. Sensor design

As mentioned in the Introduction, a number of arm-locking variants have been proposed. They differ in the way the science signals from the two arms extending from the master SC are combined to form an error signal (and of course the matching controller design that completes the control system). In the language of (14), the sensor vector **S** differs for each design. The general goal in designing the sensor vector is to make the transfer function from laser frequency noise to arm-locking sensor output as simple as possible with flat amplitude and phase responses. Ideally, $|P(f)| \approx 1$ and $\partial \angle P(f)/\partial f = 0$, where

$$P(f) \equiv \frac{\nu_{B1}(f)}{\nu_{O1}(f)}. \tag{21}$$

For example, the original proposal for single arm locking, with sensor matrix $\mathbf{S}_{\text{single}} = [\frac{1}{2}, 0]$, has $P_{\text{single}}(f) = i \sin(2\pi f \tau) e^{-2\pi i f \tau}$, where $\tau = \tau_{12} + \tau_{21}$ is the round-trip light travel time. This transfer function has nulls at frequencies $f_n = n/\tau \approx 33\ \text{mHz} \cdot n$, $n = 1, 2, 3\ldots$, a number of which lie in the LISA measurement band. Since the sensor cannot measure the frequency fluctuations at these frequencies, the control system cannot correct for them. Furthermore, the rapid swings in the transfer function phase at the f_n frequencies make it difficult to design a stable controller that extends beyond f_1. More sophisticated arm-locking sensors, such as the modified dual arm-locking sensor (MDALS) [9] make a careful blend of the two science signals to generate a sensor with a nearly flat transfer function in the measurement band.

The problem of blending of multiple sensors to generate the best possible measurement of a state variable is a classical problem in control theory. In a previous work [23], we applied Kalman filtering techniques to generate an arm-locking sensor. We will briefly review this approach here.

We begin by making a time-invariant, discrete-time linear state-space model of the LISA constellation. The state vector represents the time history of the laser frequency noise over the storage time in the arms,

$$x_k = \begin{Bmatrix} \nu_{O1}[(k-1)\Delta t] \\ \nu_{O1}[(k-2)\Delta t] \\ \vdots \\ \nu_{O1}[(k-T_{12})\Delta t] \end{Bmatrix}, \tag{22}$$

where Δt is the discretization time, k is the time index, and $T_{1j} \equiv \text{round}[(\tau_{1j} + \tau_{j1})/\Delta t]$ is the index corresponding to the round-trip light travel time between SC_1 and SC_j. We assume without loss of generality that $T_{12} > T_{13}$. Note that the first element in the state vector represents the frequency delayed by a single time step as opposed to the instantaneous frequency.

The state vector is updated using the following relations:

$$\vec{x}_{k+1} = \mathbf{A}\vec{x}_k x_k + \mathbf{B}u_k + \mathbf{\Gamma} w_k, \tag{23}$$

$$\mathbf{A} = \begin{bmatrix} 0 & 0 & 0 & \cdots & \cdots & 0 \\ 1 & 0 & 0 & \cdots & \cdots & 0 \\ 0 & 1 & 0 & \ddots & \cdots & \vdots \\ 0 & 0 & 1 & \ddots & \cdots & \vdots \\ \vdots & \vdots & \ddots & \ddots & 0 & \vdots \\ 0 & 0 & \cdots & \cdots & 1 & 0 \end{bmatrix}, \tag{24}$$

$$\mathbf{B} = \mathbf{\Gamma} = [10\cdots0]^T. \tag{25}$$

The scalar u_k represents the frequency control signal applied to the laser. In this case it would be the output of the block labeled G_1 in Fig. 1.

$$u_k = \nu_{B1}(k\Delta t) \otimes G_1, \tag{26}$$

where $\otimes$ denotes convolution. Similarly, the scalar w_k represents the instantaneous frequency noise applied to the laser at time $k\Delta t$,

$$w_k = \nu_{L1}(k\Delta t). \tag{27}$$

In other words, (23) says that the laser control signal and the laser noise effect only the first element of the state vector and the remaining elements are determined through simple time delays.

The two frequency meter outputs can be combined to form a two-element measurement vector, $\vec{y}_k$ which is determined from the following relation:

$$y_k \equiv \begin{bmatrix} \nu_{A12}(k\Delta t) \\ \nu_{A13}(k\Delta t) \end{bmatrix} = \mathbf{C}\vec{x}_k + \mathbf{D}u_k + \mathbf{H}w_k + \vec{n}_k, \tag{28}$$

$$\mathbf{C} = \begin{bmatrix} 0 & 0 & \cdots & \cdots & \cdots & -1 \\ 0 & \cdots & 0 & -1 & 0 & \cdots \end{bmatrix}, \tag{29}$$

$$\mathbf{D} = \mathbf{H} = \begin{bmatrix} 1 \\ 1 \end{bmatrix}. \tag{30}$$

C is a $2 \times T_{12}$ matrix describing how the state vector couples into the frequency meter measurements. All elements of **C** are zero with the exception of $(1, T_{12})$ and

(2, T_{13}), which are -1. This represents the fact that the frequency meter measurement includes a copy of the master laser phase delayed by the round-trip light travel time in the arm. The 2×1 vector $\vec{n}_k$ represents the noise in each of the two frequency meter signals at the current time step. This includes the shot noise, clock noise, and spacecraft jitter noise contributions. The noise level can be determined from the noise spectra in Sec. II F and the transfer functions to frequency meter outputs in (13).

Equations (23) and (28) are the classical state-space description of a linear system. Kalman filtering [24,25] is a prescription for generating an optimal estimate of the state vector provided information about the system matrices and noise processes are available. In our case, the state matrices are determined by the arm-lengths (through the definitions of T_{12} and T_{13}) and the noise models that determine w_k and $\vec{n}_k$. The output of the Kalman filter is an estimate of the state vector, $\vec{x}_k$, the first element of which corresponds to the laser frequency at time $(k-1)\Delta t$. This element is the output of our Kalman-filter based sensor, which we refer to as an optimal arm-locking sensor or OALS.

In Fig. 3, we show a comparison of the transfer function from laser frequency noise to sensor output for the single-arm, MDALS, and OALS designs. The round-trip arm lengths were chosen to be 33 s and 32.4 s for all three sensors for direct comparison purposes. There is no specific significance to the choice. The OALS sensor was computed with $\Delta t = 0.1$ s and perfect arm-length knowledge was assumed for both MDALS and OALS. When compared with the single-arm sensor, both MDLAS and OALS exhibit much flatter responses in the LISA measurement band. This allows arm-locking systems based on them to achieve more uniform suppression, particularly near the round-trip frequencies. The OALS has less ripple than the MDALS at frequencies below ~100 mHz but reaches a peak in-band ripple around 300 mHz which is similar to that of MDALS. Both sensors can be used to build arm-locking systems that meet the LISA performance criteria. The OALS is optimal in the sense that it is generated using optimal control theory techniques. When paired with a suitable controller, we find that the net system performance is similar to that achieved with the MDALS sensor, which gives us some confidence in that design.

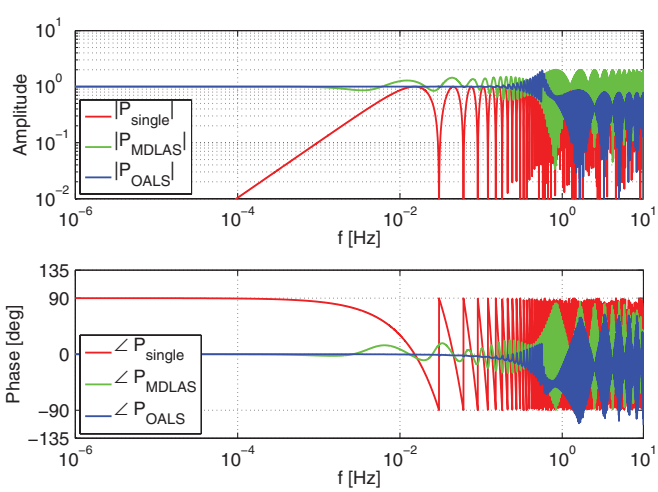

FIG. 3 (color). Transfer function from master laser frequency noise to sensor output for various arm-locking sensors: Single-arm sensor [7], MDALS [9], and OALS (this work). For all cases, the round-trip light travel times in the two arms are 33 s and 32.4 s.

B. Controller design

The second component in an arm-locking system is a controller, which takes the estimate of the laser frequency provided by the arm-locking sensor and generates a frequency tuning command for the laser. The design goals of the controller are to provide sufficient gain within the LISA measurement band to suppress the intrinsic frequency fluctuations of the master laser (15) below the levels tolerated by TDI (1). As mentioned in Sec. III, care must also be taken to minimize the controller gain at very low (below measurement band) frequencies to mitigate laser frequency pulling.

The controller is based on a classical lead-lag design. It includes a second-order lead filter at the lower frequencies (break frequency at 0.05 mHz) to abate laser pulling due to uncompensated Doppler and Doppler derivative. It also includes a shaping filter and a single-order attenuation filter at 4 Hz to limit the controller action to the LISA band. Figure 4 contains a Bode plot of the controller.

C. Simulation design

We implemented a discrete-time simulation of arm locking as described in the preceding sections using the SIMULINK software package. Each arm was modeled in a manner consistent with Sec. II. The round-trip arm lengths were assumed to be $\tau_{12} + \tau_{21} = 33$ s$/c$ and

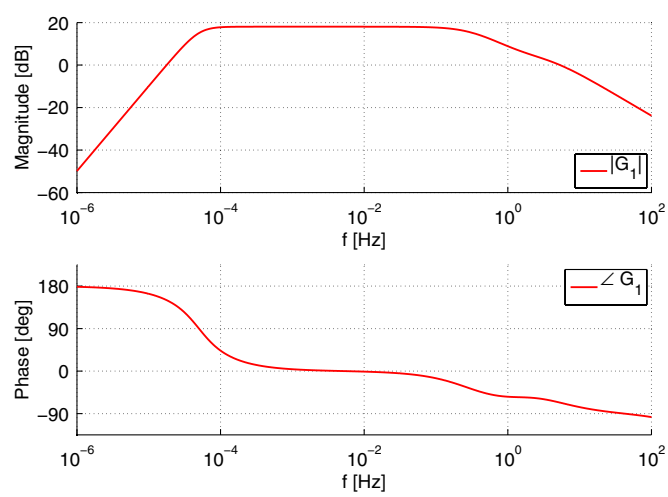

FIG. 4 (color online). Bode plot of arm-locking controller.

$\tau_{13} + \tau_{31} = 32.4$ s/c, where c is the speed of light. The phase-lock loops on SC_2 and SC_3 were assumed to be perfect ($G_2 = G_3 \gg 1$) with constant frequency offsets ($\nu_{M21} = 10$ MHz, $\nu_{M31} = 15$ MHz). The Doppler shifts in each arm were modeled as a linearly varying frequency with the coefficients provided by the orbital model in Fig. 2 at a time $t = 1$ yr. Doppler errors were linear in time with the coefficients provided in Table I. The spectrum of intrinsic frequency fluctuations in the laser systems was modified from (15) to include two poles at 0.6 μHz, limiting the total frequency excursion to $\sim$(20 MHz) over the maximum simulation period of two weeks. A two pole roll-off at 0.5 Hz was added to the spacecraft jitter noise in (7) to model the dynamics of the SC above the measurement band.

The simulation cadence was 500 μs. System dynamics, noise generators, and the controller operated at this cadence. The OALS was implemented with the designed 10Hz sampling rate, with appropriate downsampling and upsampling filters providing the rate transitions. The OALS filter order was also reduced from the nominal order of 332 to 38 using balanced reduction [26]. This reduction provides a dramatic increase in simulation speed without changing the behavior in the LISA measurement band.

V. RESULTS

A. Component noise sources

The first goal of the time-domain simulation was to verify the analytic, frequency-domain model of the arm-locking system. Figure 5(a) contains a noise decomposition of the OALS arm-locking system derived from an analytic model. As can be seen, the overall noise in the stabilized laser is dominated by residual laser frequency noise, with the other noise sources being nearly 4 orders of magnitude smaller. Figure 5(b) shows a similar plot obtained using the time-domain simulations. To obtain each curve, the simulation was run with all noise sources except the source of interest turned off. In all cases, the Doppler estimation errors were set to zero. The time series were then used to estimate a spectra. The two plots show good agreement over most of the LISA band. The primary differences are a broadening of the sharp spectral features near $f = n/\tau$ and a roll-off at low frequencies in the time-domain plots. Both of these effects are consistent with spectral estimation errors in the logarithmic power spectral density algorithm [27] used to compute the spectra from the time series outputs.

B. Laser frequency pulling

The second goal of the time-domain simulations was to explore phenomena that are not easily treated analytically in the frequency domain. The laser frequency pulling described in Sec. III is an important example of such a phenomenon. We ran a simulation spanning two full weeks (the expected time between SC maintenance periods) with Doppler estimation errors consistent with our models of the errors in the averaging method. Figure 6 shows the results of this simulation. In the top panel, there are two curves plotted: the frequency change of the arm locked system and the frequency change of the intrinsic MZ noise. The first thing to notice is that the arm locked system drifts over approximately 20 MHz over the two week simulation period, well within the expected linear tuning range of the LISA lasers. The second thing to notice is that the

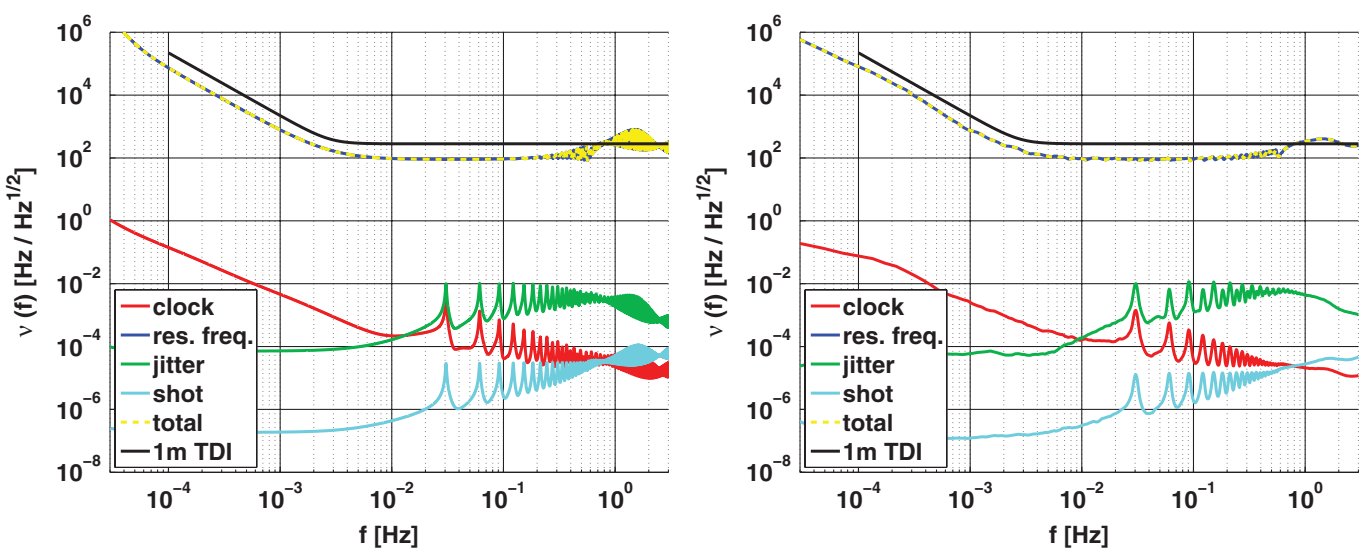

FIG. 5 (color). Noise decomposition of the OALS arm-locking system derived from a frequency domain model (left) and a time domain model (right). For both models, the noise contributions below 10 mHz are, in order from the lowest: shot noise, jitter, and clock noise. The total noise estimate is dotted and lies on top of the residual frequency noise measurement just below the solid curve that represents the capability of TDI with a 1 meter range error.

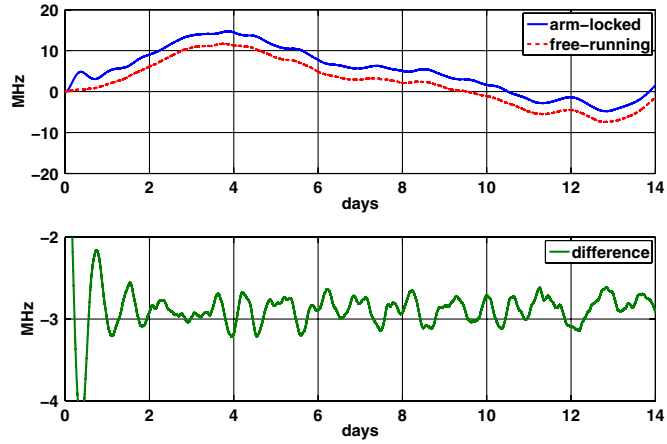

FIG. 6 (color online). Top panel: comparison of arm locked laser frequency drift with intrinsic laser frequency drift. Bottom panel: Difference of the two curves in the upper panel giving a rough estimate of the contribution to laser frequency drift from the arm-locking system.

frequency drift in the arm locked system is approximately equal to the drift in the intrinsic noise. This is due to the fact that the arm-locking loop has no effect below the LISA measurement band. The lower panel plots the difference of the arm locked and intrinsic frequency drifts, which gives an indication as to the level of additional drift generated by the arm-locking system. After an initial transient decays over the first few days, the remaining fluctuations are less than 1 MHz. This demonstrates that this arm-locking design does not produce any significant pulling of the master laser frequency beyond what is already present in the MZ stabilization system.

C. Robustness to arm-length errors

Like the MDALS sensor, the OALS sensor requires some *a priori* knowledge of the LISA arm lengths. Many of the same techniques described in Sec. III B that can potentially be used for estimating the Doppler frequencies can also be applied to estimate arm lengths. Which technique is most applicable will depend on how sensitive the performance of the arm-locking system is to errors in the estimated arm lengths used to compute the sensor. For example, if the maximum tolerable error is $\sim$1 m then active ranging is likely the best candidate. If, on the other hand, errors of $\sim$10 km are tolerable, it may be possible to compute them from orbital ephemerides on the ground and upload new coefficients to the OALS periodically.

To check the robustness of the OALS to errors in the arm length, we first define the mean and differential arm lengths assuming SC_1 is the master SC,

$$\tau_m \equiv \tfrac{1}{2}[\tau_{12} + \tau_{21} + \tau_{13} + \tau_{31}], \tag{31}$$

$$\delta\tau \equiv [\tau_{12} + \tau_{21} - \tau_{13} - \tau_{31}]. \tag{32}$$

We then design an OALS for a specific set of nominal arm lengths, $\tau_m^{(0)} = 32.85$ s and $\delta\tau^{(0)} = 0.3$ s, corresponding to the constellation geometry at $t \approx 1.25$ yrs in the orbital solution used in Fig. 2. This sensor is used to stabilize an array of arm-locking systems with different true arm lengths, which corresponds not only to an error in the determination of the true arm lengths, but also represents the situation where the spacecraft constellation has evolved in time away from the design point. To quantify the effect of arm-length errors, we define the figure of merit.

$$\Psi_0(\tau_m, \delta\tau) \equiv 20\log_{10}\left[f \max \frac{\tilde{\nu}_{\text{pre-TDI}}(f)}{\tilde{\nu}_{O1}(f, \tau_m, \delta\tau)}\right], \tag{33}$$

where $\tilde{\nu}_{O1}(f, \tau_m, \delta\tau)$ is the residual noise in the master laser and $\tilde{\nu}_{\text{pre-TDI}}(f)$ is the residual noise requirement specified in (1). Ψ_0 measures the minimum margin in the LISA measurement band between the arm-locking system and the pre-TDI requirement. Where this minimum is positive, the frequency stabilization is guaranteed to meet performance requirements.

Figure 7 shows a contour plot of Ψ_0 for this example plotted on the $(\tau_m, \delta\tau)$ plane. The design point $[\tau_m^{(0)}, \delta\tau^{(0)}]$ is indicated by a white diamond. The evolution of τ_m and $\delta\tau$ due to the LISA orbit near the design is indicated by the dashed line with the grey dots indicating time intervals of

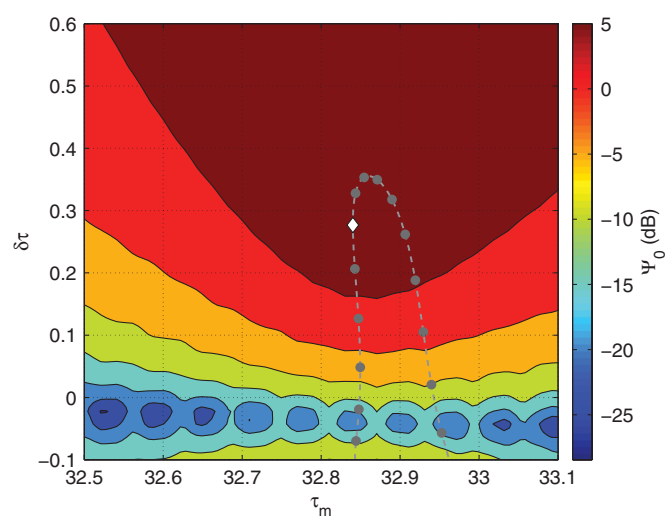

FIG. 7 (color). Robustness of an example OALS-based arm-locking system to errors in arm-length versus the mean (τ_m) and differential ($\delta\tau$) arm-lengths. The contours show Ψ_0, the minimum margin in any given frequency bin within the LISA measurement band. The white diamond marks the design point for the sensor and the dashed line shows the evolution of the arm lengths due to LISA orbital motion near the design point with the grey dots spaced in time by 15 days. The dark red color shows a positive margin between 0 and 5 dB indicating that the performance of the system meets or exceeds the requirement. Evolution of the system is from left to right, indicating that the system has adequate performance from approximately 20 days before the design point to approximately 100 days after.

15 days. Figure 7 shows that the positive margin exists for ~20 days prior to the design point and ~100 days afterwards. This is much larger than the expected intervals between maintenance activities, indicating that updating the OALS sensor coefficients will not drive the maintenance schedule of the mission. The existence of a large operating window gives us some confidence that the OALS design is robust enough for the LISA application.

When arm-length errors eventually do cause the system performance to degrade to the point where the margin is inadequate, it will be necessary to change the OALS coefficients and possibly which SC is designated as the master. Changing the coefficients can likely be done smoothly without losing lock or degrading system performance. Changing the master SC will require reconfiguring of the phase-lock loops aboard all SC and will result in some down time. This should only be required when $\delta\tau$ for a certain arm combination becomes sufficiently small, likely 1–3 times per year.

VI. CONCLUSIONS

Arm Locking is a candidate laser frequency stabilization technique for LISA. We have used a time-domain simulation to study a design for an arm-locking system based on a Kalman-filter optimal blended sensor and a controller which meets the frequency stability requirements for LISA assuming the master laser is prestabilized to a level of 800 $\mathrm{Hz}/\sqrt{\mathrm{Hz}}$. Time-domain simulations allowed us to study transient phenomena and the performance of the stabilization system as the conditions of the LISA constellation evolve during the normal orbital motion, including Doppler shifts and imperfectly known arm lengths. The simulations indicate that it is possible to implement arm locking without excessive pulling of the master laser frequency, and that the arm-locking sensor performance is robust against errors in the absolute arm-length estimates. This robustness allows the sensor to be periodically updated with precomputed filter coefficients at intervals that are operationally reasonable. Although our time-domain simulation necessarily included specific sensor and controller designs, the same simulation infrastructure could be applied to study other candidate sensor and controller designs.

ACKNOWLEDGMENTS

We would like to thank Kirk McKenzie for providing the tools needed to compute the MDALS arm-locking performance and Steve Hughes for providing LISA orbital data.

APPENDIX: KEY TO NOTATION

TABLE II. Partial key to notation and comparison with [9].

Symbol	Description	Correspondence in [9]
$G_i(s)$	controller transfer function on SC_i	$G_i(s)$
$\mathbf{S}$	arm-locking sensor vector	$\mathbf{S}$
$\vec{V}_i$	total velocity of SC_i	N/A
$\vec{V}_{Qi}$	orbital component of SC_i velocity	N/A
$\delta\vec{V}_i$	jitter component of SC_i velocity	$(\delta\vec{V}_i - \delta\vec{V}_j)\cdot\hat{\eta}_{ij} = \frac{\partial}{\partial t}\Delta X_{ij}$
$\tilde{y}_i(f)$	fractional frequency fluctuations of SC_i clock	$\tilde{y}_i(f)$
$\hat{\eta}_{ij}$	unit vector from SC_i to SC_j	N/A
λ	wavelength of lasers	λ
ν_{Aij}	output of frequency meter ij	$\frac{\partial}{\partial t}\phi_{Aij}$
ν_{B1}	output of arm-locking sensor	$\frac{\partial}{\partial t}\phi_{B1}$
ν_{Cij}	clock noise generated by frequency meter ij	$\frac{\partial}{\partial t}\phi_{Cij}$
ν_{Dij}	orbital Doppler shift measured by frequency meter ij	N/A
ν_{E1j}	error in heterodyne model	$\nu_{\mathrm{DE}1j}$
ν_{Hij}	heterodyne signal at photoreceiver ij	N/A
ν_{Jij}	spacecraft jitter Doppler shift at measurement ij	$\frac{\partial}{\partial t}\phi_{Xij}$
ν_{Li}	intrinsic frequency noise of Laser i	$\frac{\partial}{\partial t}\phi_{Li}$
ν_{Mij}	heterodyne model signal on frequency meter ij	$\Delta_{i1} i = 2, 3$
$\nu_{M+(-)}$	model of common (differential) component of heterodyne signals on SC_1	N/A
$\nu_{0+(-)}$	constant part of $\nu_{M+(-)}$	$\nu_{0+(-)}$
$\gamma_{0+(-)}$	linear part of $\nu_{M+(-)}$	$\gamma_{0+(-)}$
$\alpha_{0+(-)}$	quadratic part of $\nu_{M+(-)}$	$\alpha_{0+(-)}$
ν_{Oi}	frequency output of Laser i	$\frac{\partial}{\partial t}\phi_{Oi}$
ν_{Sij}	shot noise at photoreceiver ij	$\frac{\partial}{\partial t}\phi_{Sij}$
τ_{ij}	light travel time from SC_i to SC_j	τ_{ij}

[1] P. Bender, K. Danzmann, and LISA Study Team, Max-Planck-Institut fur Quantenoptik, Garching Technical Report No. MPQ233, 1998, http://lisa.gsfc.nasa.gov/Documentation/ppa2.08.pdf.
[2] O. Jennrich, Classical Quantum Gravity **26**, 153001 (2009).
[3] J. Armstrong, F. Estabrook, and M. Tinto, Astrophys. J. **527**, 814 (1999).
[4] D. Shaddock, M. Tinto, F. Estabrook, and J. Armstrong, Phys. Rev. D **68**, 061303(R) (2003).
[5] D. Shaddock *et al.*, Report No. LISA-JPL-TN-823, Laser Interferometer Space Antenna, 2009 (unpublished).
[6] J. Thorpe, Classical Quantum Gravity **27**, 084008 (2010).
[7] B. Sheard, M. Gray, D. McClelland, and D. Shaddock, Phys. Lett. A **320**, 9 (2003).
[8] A. Sutton and D. Shaddock, Phys. Rev. D **78**, 082001 (2008).
[9] K. McKenzie, R. E. Spero, and D. A. Shaddock, Phys. Rev. D **80**, 102003 (2009).
[10] B. Sheard, M. Gray, D. Shaddock, and D. McClelland, Classical Quantum Gravity **22**, S221 (2005).
[11] A. G. Marin *et al.*, Classical Quantum Gravity **22**, S235 (2005).
[12] V. Wand *et al.*, J. Phys. Conf. Ser. **154**, 012024 (2009).
[13] D. Shaddock, Classical Quantum Gravity **25**, 114012 (2008).
[14] D. Shaddock *et al.*, *Proceedings of the Sixth International LISA Symposium*, edited by S. Merkowitz and J. Livas (AIP Conference Proceedings, New York, 2006), Vol. 873, pp. 654–660.
[15] F. Steier *et al.*, Classical Quantum Gravity **26**, 175016 (2009).
[16] M. Armano *et al.*, Classical Quantum Gravity **26**, 094001 (2009).
[17] W. Klipstein *et al.*, in *Laser Interferometer Space Antenna: 6th International LISA Symposium*, edited by S. Merkowitz and J. Livas (AIP Conference Proceeding, New York, 2009), Vol. 873, pp. 312–318.
[18] P. Maghami and T. Hyde, Classical Quantum Gravity **20**, S273 (2003).
[19] S. Hughes, J. Guid. Control. Dyn. **31**, 414 (2008).
[20] C. Thornton and J. Border, *Radiometric Tracking Techniques for Deep-Space Navigation*, Deep-Space Communications and Navigation Series (John Wiley & Sons, Hoboken, 2005).
[21] J. J. Esteban *et al.*, J. Phys. Conf. Ser. **228**, 012045 (2010).
[22] G. Heinzel, Classical Quantum Gravity **28**, 094008 (2011).
[23] P. Maghami, J. Thorpe, and J. Livas, *Proceedings of the SPIE Symposium on Advanced Wavefront Control: Methods, Devices, and Applications VIII* (SPIE, San Diego, 2009), Vol. 7466, pp. M1–M11.
[24] R. Stengel, *Stochastic Optimal Control: Theory and Application* (John Wiley & Sons, New York, 1986).
[25] C. Phillips and H. Nagle, *Digital System Analysis and Design* (Prentice Hall, Englewood Cliffs, NJ, 1995), 3rd ed.
[26] J. Maciejowski, *Multivariable Feedback Design* (Addison-Wesley, Boston, 1989).
[27] M. Tröbs and G. Heinzel, Measurement **39**, 120 (2006).